Supplementary information to

Albumin protein encapsulation into ZIF-8 framework with Co-LDH-based hierarchical architectures for robust catalytic reduction

Maryam Chafiq [1], Abdelkarim Chaouiki [1,*], Tri Suhartono, Young Gun Ko [*]

Materials Electrochemistry Group, School of Materials Science and Engineering,
Yeungnam University, Gyeongsan 38541, Republic of Korea

[1] These authors contributed equally to this work

*Corresponding authors.
E-mail addresses: abdelkarim.chaouiki@yu.ac.kr (A. Chaouiki) , younggun@ynu.ac.kr (Y.G. Ko)

The materials include content:

Supplementary Figs 1 to 22

Supplementary Table

Supplementary discussion

Methods section

Supplementary References

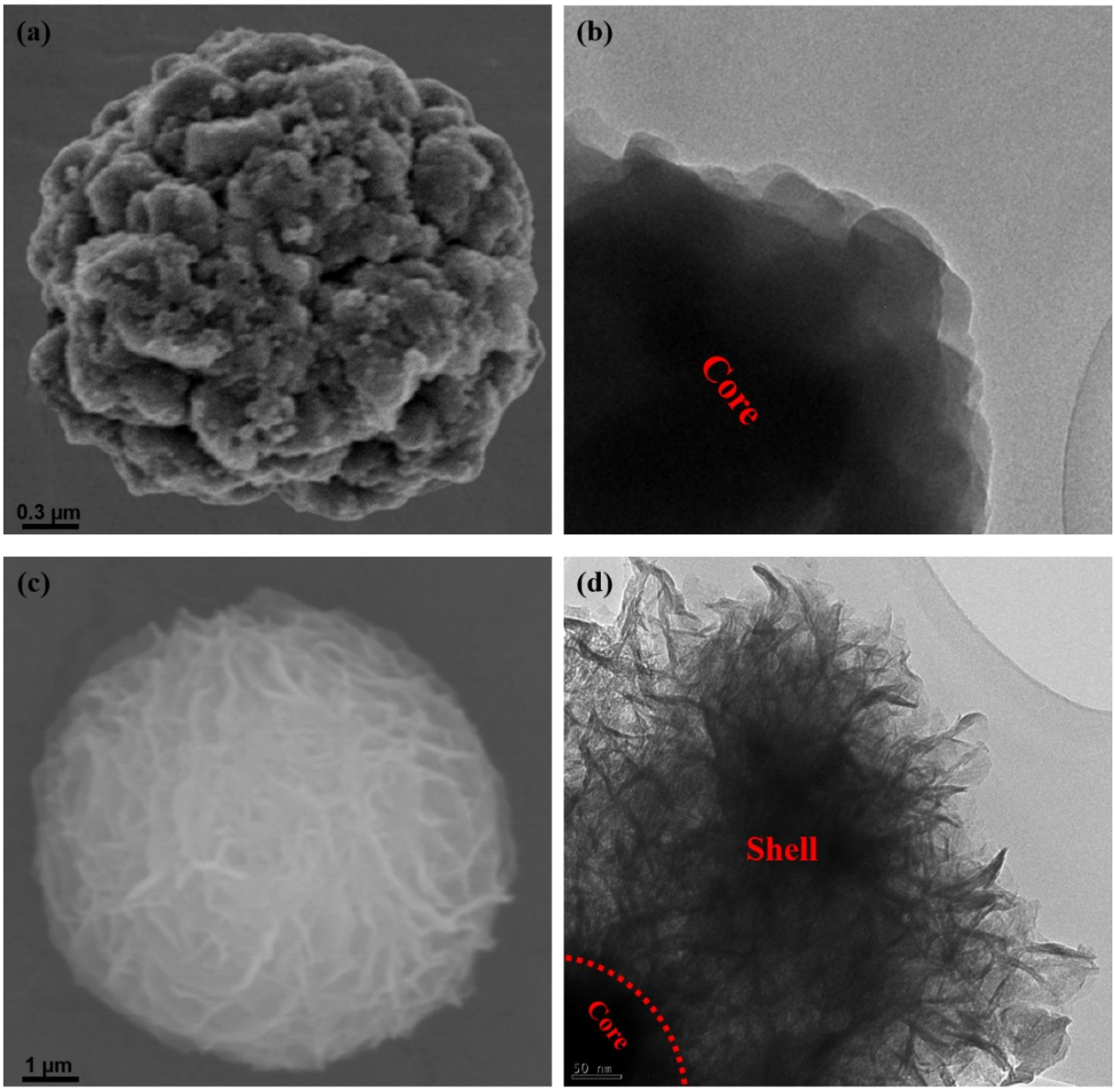

Fig. S1: Characterization of final (a, b) Pro@ZIF-8 and (c, d) Pro@ZIF-8-LDH nanocomposites. (a, c) SEM and (b, d) TEM images, showing the interface of the heterojunction between Co-LDH and Pro@ZIF-8.

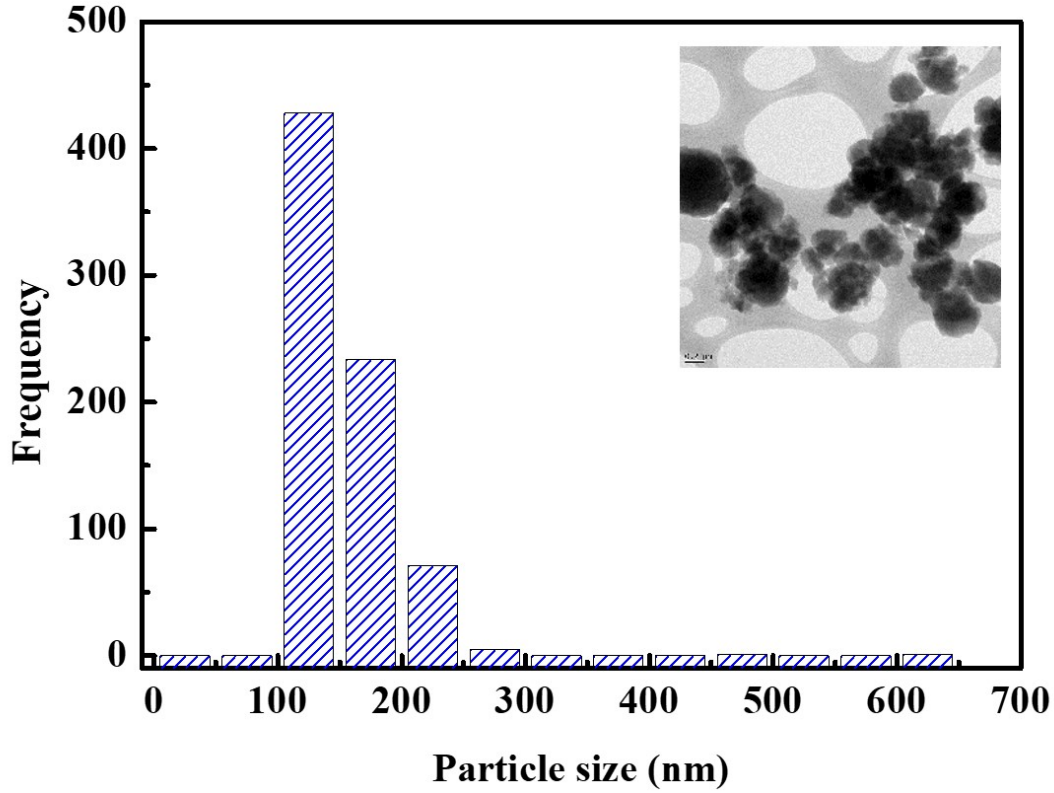

Fig. S2: Size distribution of Pro@ZIF-8 nanocomposite.

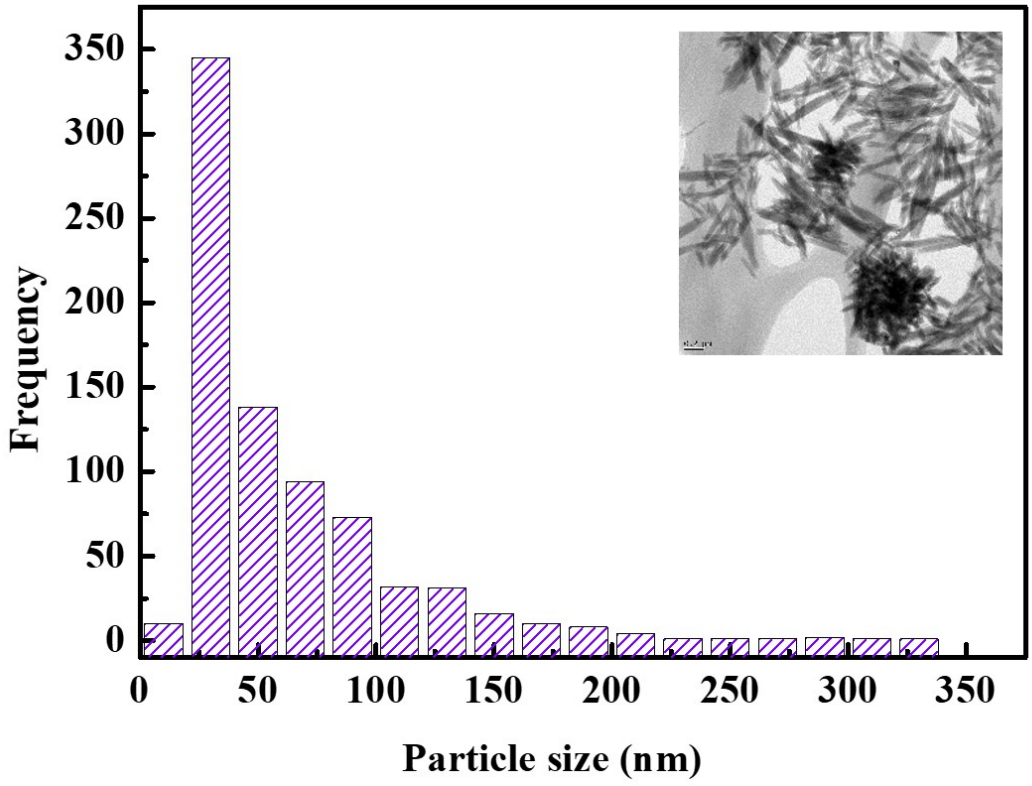

Fig. S3: Size distribution of Co-LDH nanoparticles.

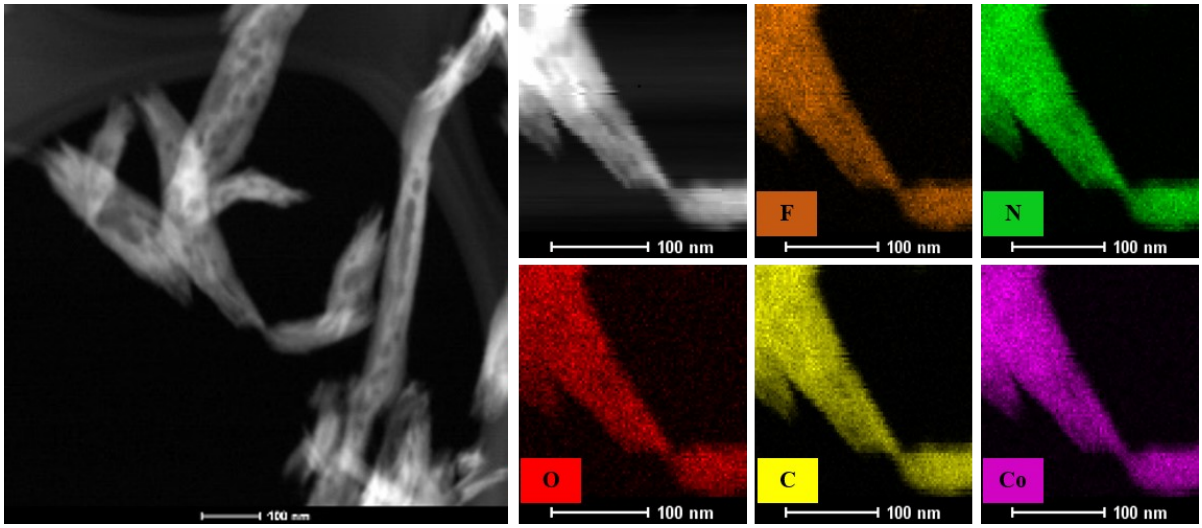

Fig. S4: Scanning transmission electron microscopy image and the corresponding element mapping of Co-LDH composite.

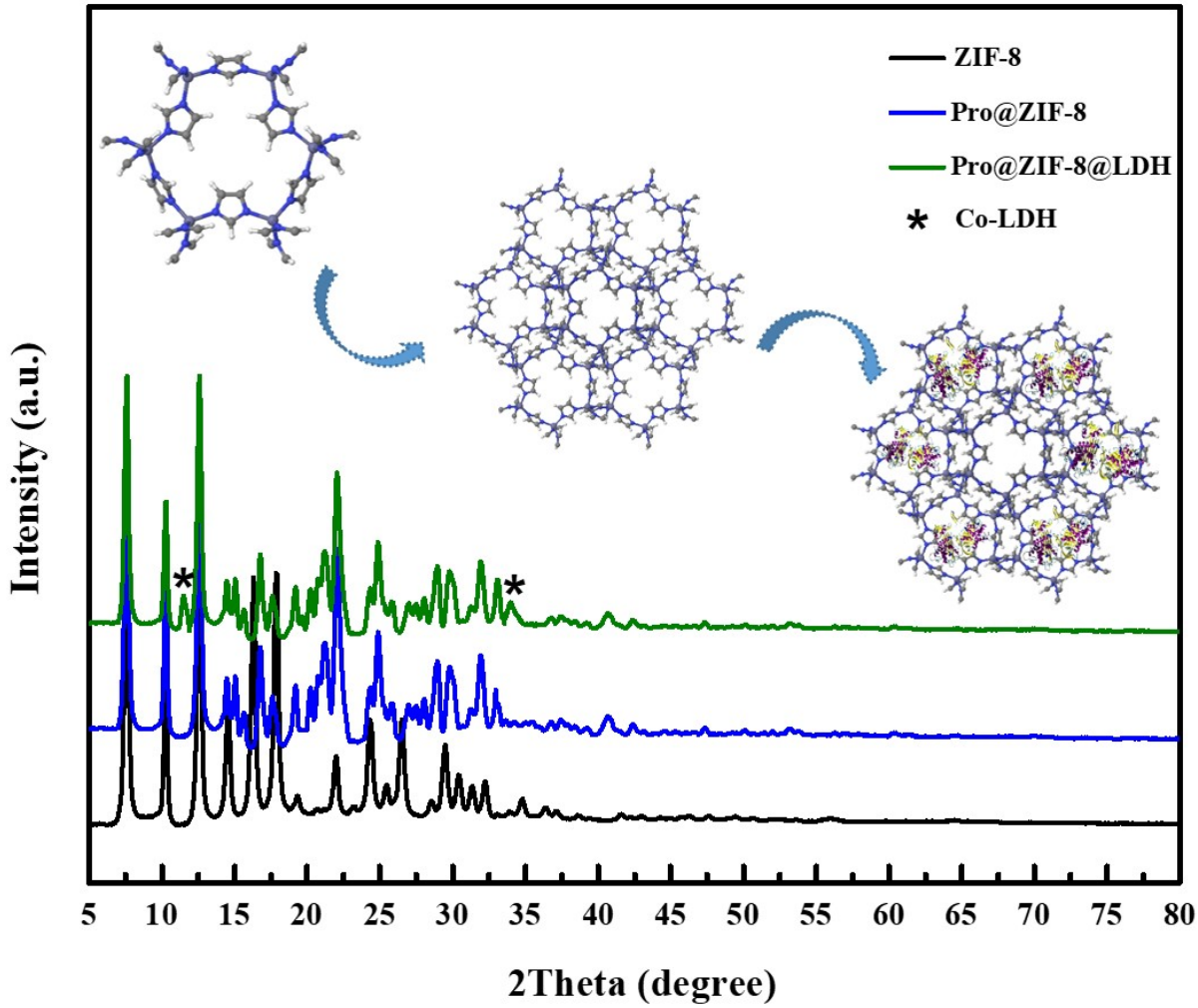

Fig. S5: XRD patterns of ZIF-8, Pro@ZIF-8, and Pro@ZIF-8-LDH materials.

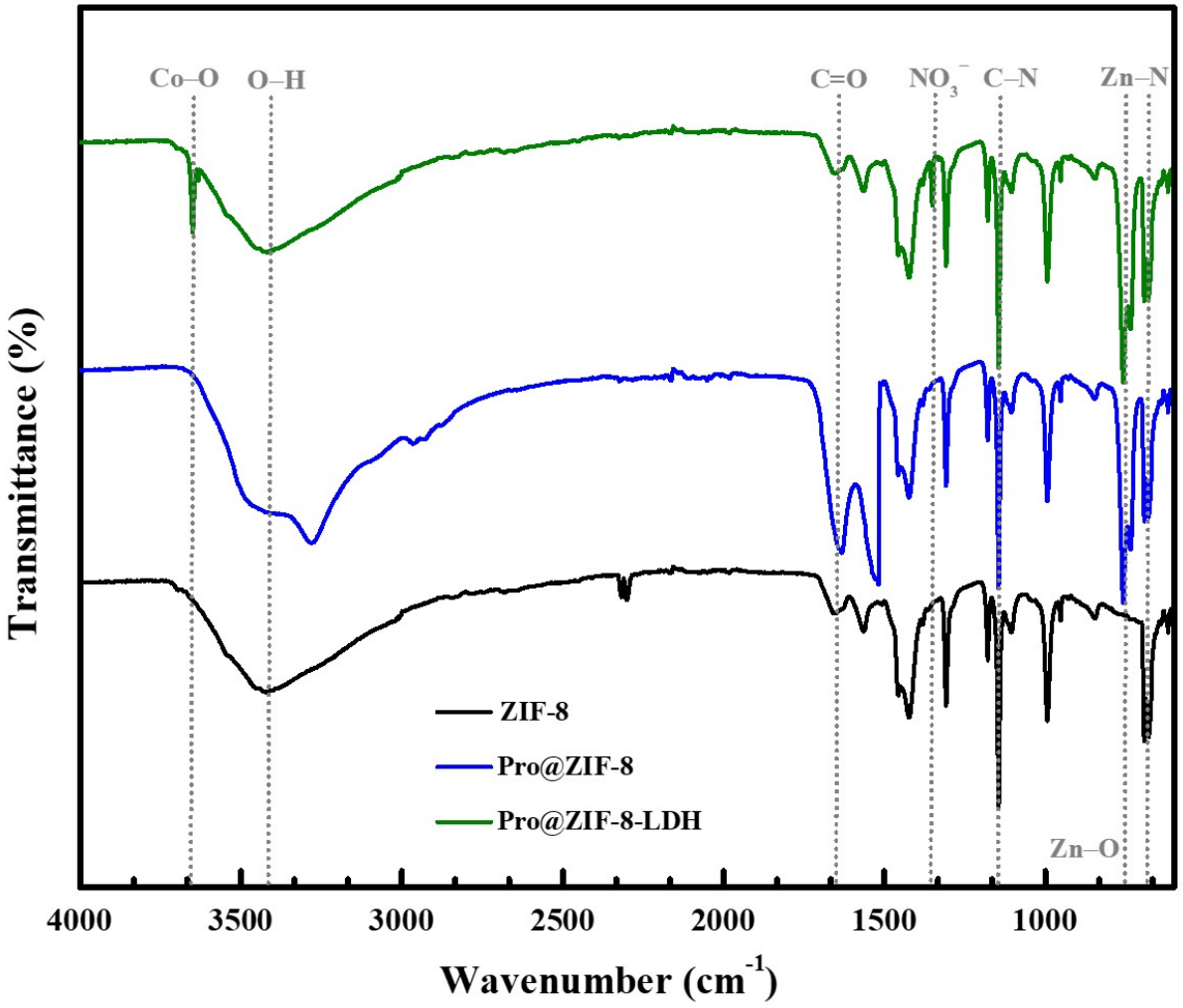

Fig. S6: FT-IR spectra of as-synthesized materials ZIF-8, Pro@ZIF-8, and Pro@ZIF-8-LDH.

To gain more insight into the encapsulation and shell protection strategies we proposed, the XRD partners and FT-IR data of ZIF-based materials (ZIF-8, Pro@ZIF-8, and Pro@ZIF-8-LDH) were conducted. The as-synthesized materials were analyzed for their compositional features using XRD measurements, and the results are presented in Fig. S5. The XRD pattern of ZIF-8 exhibited a characteristic set of sharp peaks, whereas the Co-LDH product produced broadened peaks at approximately 11.4° and 33.9°, corresponding to the (003) and (009) facets, respectively [1,2]. These observations are consistent with those reported in the literature [3], providing evidence for the successful formation of LDH materials on the interface of the ZIF material [4–6]. This compositional variation suggests that the LDH material was successfully incorporated onto the ZIF-8 surface, leading to a unique hybrid material with potentially enhanced properties. These results highlight the importance of understanding the compositional features of materials and their impact on their properties, which is crucial in the

development of advanced materials for various applications.

The Fourier transform infrared spectroscopy spectra of the three as-prepared materials were obtained to further investigate the interface interaction between ZIF-8 and Co-LDH. Fig. S6 in the Supporting Information shows two absorption peaks of ZIF-8 (680 and 990 cm^{-1}) in all samples [7,8], proving the integrity of ZIF-8 after encapsulation [9–11]. For the pristine ZIF-8, several characteristic peaks were observed, as shown in Fig. S6. For example, absorption bands at 1135 cm^{-1} is assigned to vibrations of C−N in the imidazole ring[12–15], in addition to a peak at 675 cm^{-1}, which belongs to Zn−N stretching as the zinc atoms in the ZIF-8 structure connect to nitrogen atoms of 2-Mim linker during the formation of ZIF-8 [16,17]. These peaks were also found in Pro@ZIF-8 and Pro@ZIF-8-LDH samples, confirming the successful fabrication of ZIF-8 material in all synthesis stages. Additionally, the symmetric stretching vibration of the N–O bond was detected in the FT-IR spectra of the LDH layers. This band resulted from the intercalation of NO_3^- anions within the interlayer of the LDH structure. Meanwhile, a new peak at about 758 cm^{-1} appeared and was attributed to stretching vibrations of Zn−O. These results indicate that the presence of protein changes the reaction mechanism, from the formation of Zn−N alone (pristine ZIF-8) to the formation of both Zn−N and Zn−O (Pro@ZIF-8) by first capturing Zn atoms and then allowing the complex to interact with 2-Mim, which is consistent with previous reports [18,19]. On other hand, the peak of Co-LDH at 3655 cm^{-1} was attributed to the stretching vibration of Co–O, while the peak at 1356 cm^{-1} was related to the N–O stretching vibration of the anion of the nitrate inserted into the layer [20,21]. As expected, the vibrational peak of Pro@ZIF-8-LDH consisted of those of Co-LDH, Pro@ZIF-8, and pristine ZIF-8. When compared with ZIF-8, the peaks at around 2300 cm^{-1} that are characteristic of the ZIF-8 spectrum were not observed, and the peak at 1630 cm^{-1} of the in-plane bending mode of the C=O fragment pathways was weakened due to the interfacial effect between Co-LDH and ZIF-8 [22–24].

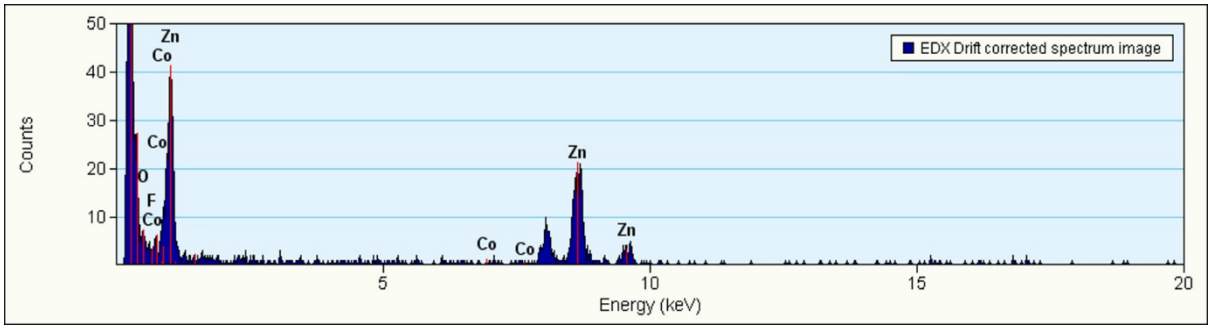

Fig. S7: EDS analysis conducted in the observed area (Fig. 2j) of Pro@ZIF-8-LDH system.

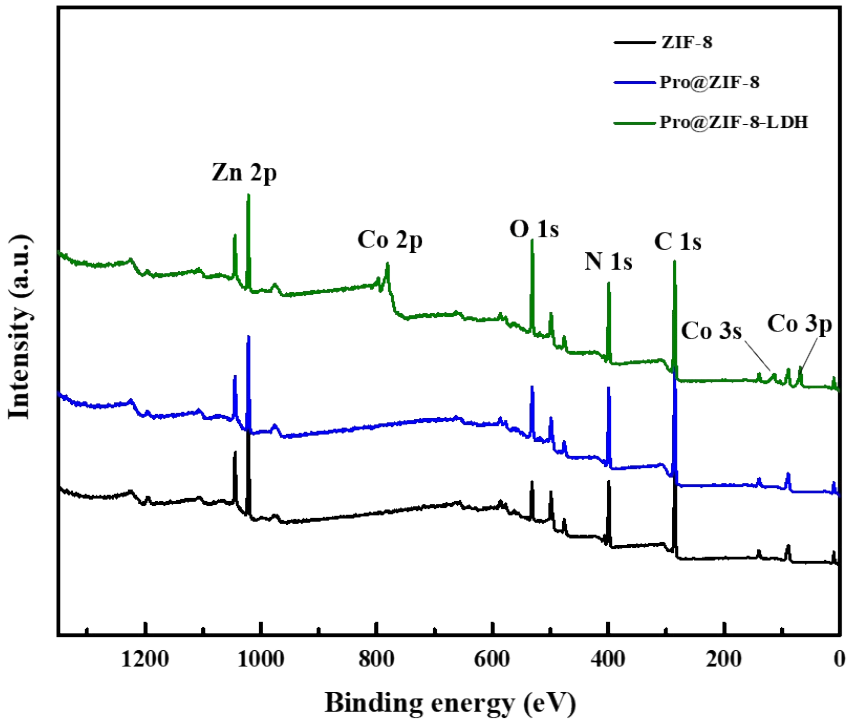

Fig. S8: XPS survey spectra confirming the elements Zn, Co, C, N and O.

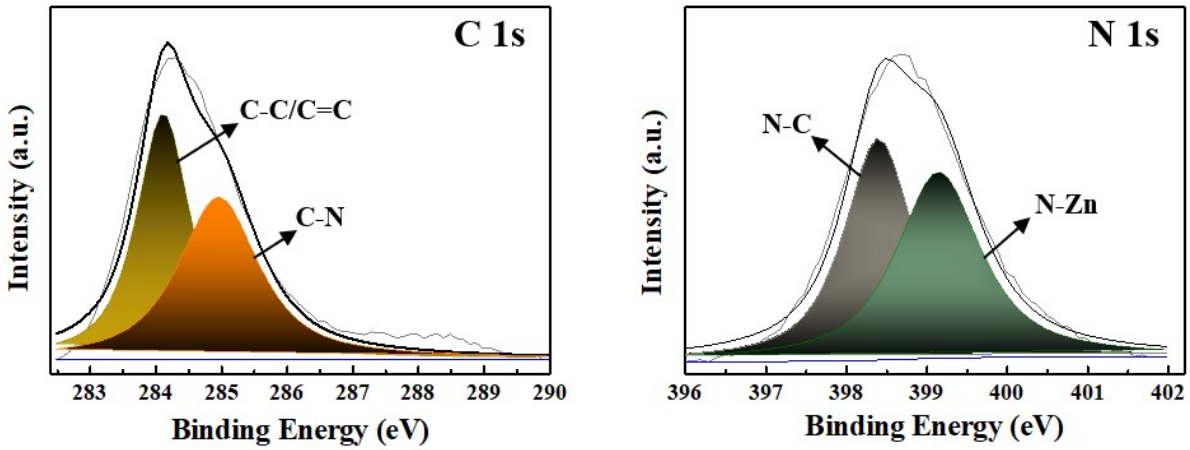

Fig. S9: High-resolution XPS spectra of carbon and nitrogen in ZIF-8 framework.

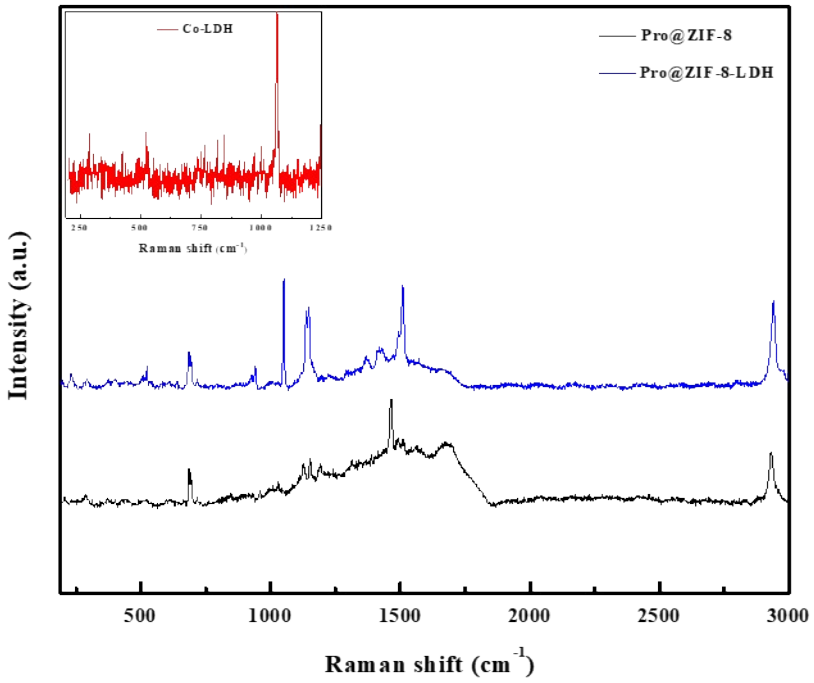

Fig. S10: Raman spectroscopy analysis of Pro@ZIF-8 and Pro@ZIF-8-LDH. The inset shows Raman spectrum of Co-LDH material.

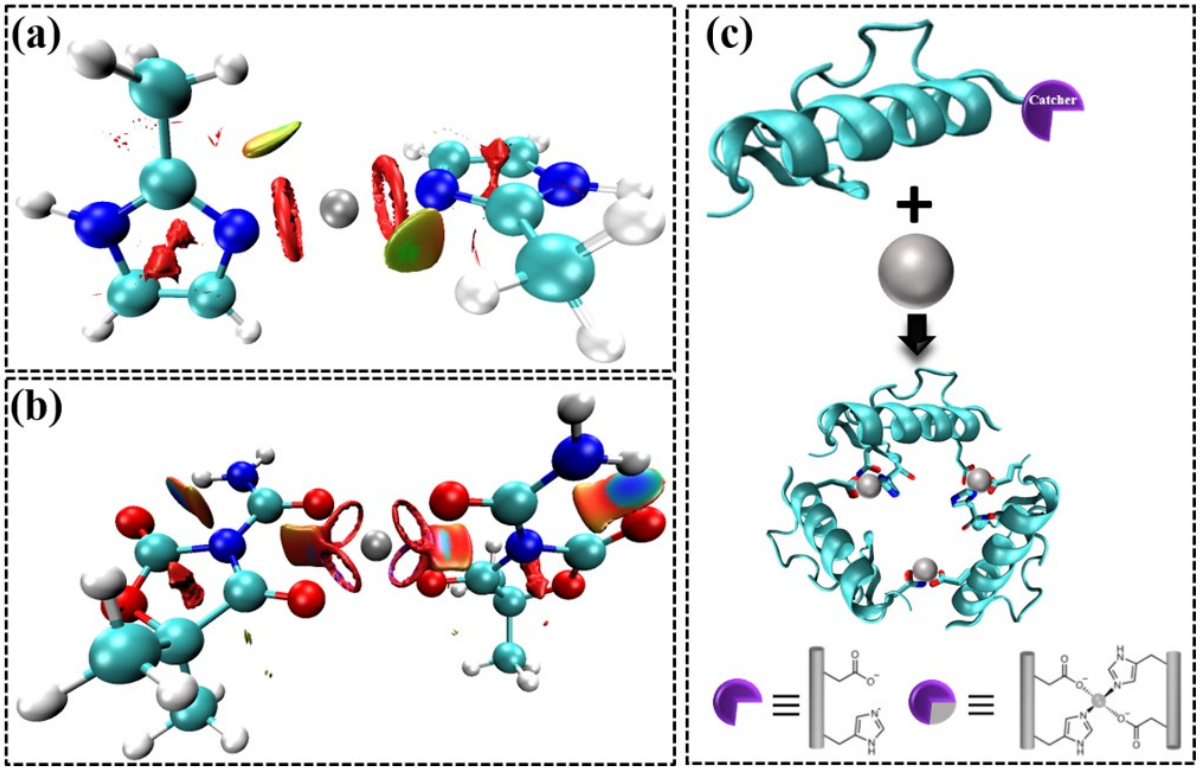

Fig. S11: Schematic illustrating the encapsulation process of Pro in ZIF-8 structure, indicating the primary bonding between (a) 2-Mim, (b) Pro, and Zn cation as demonstrated by DFT calculations.

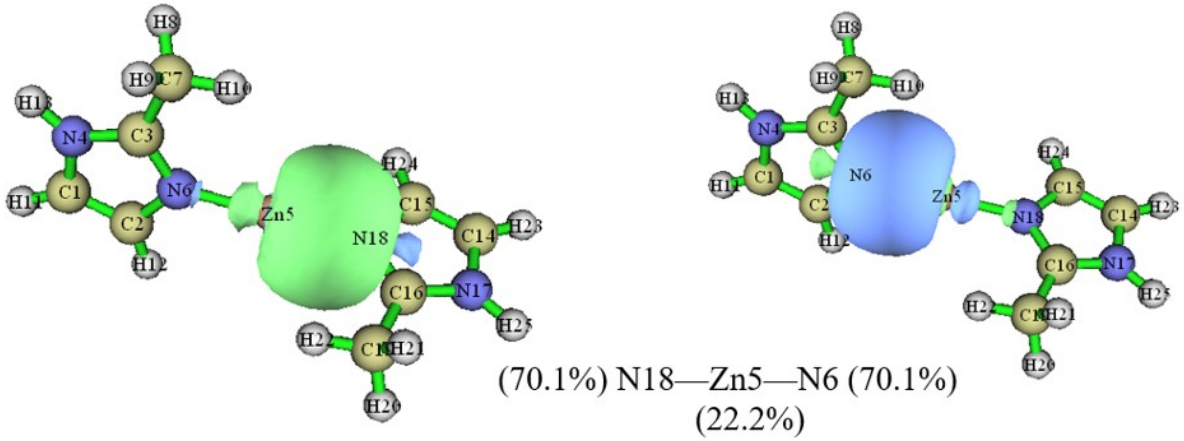

Fig. S12: Distribution of localized molecular orbitals in $Zn(2\text{-}Mim)_2$ system as calculated by LMO analysis.

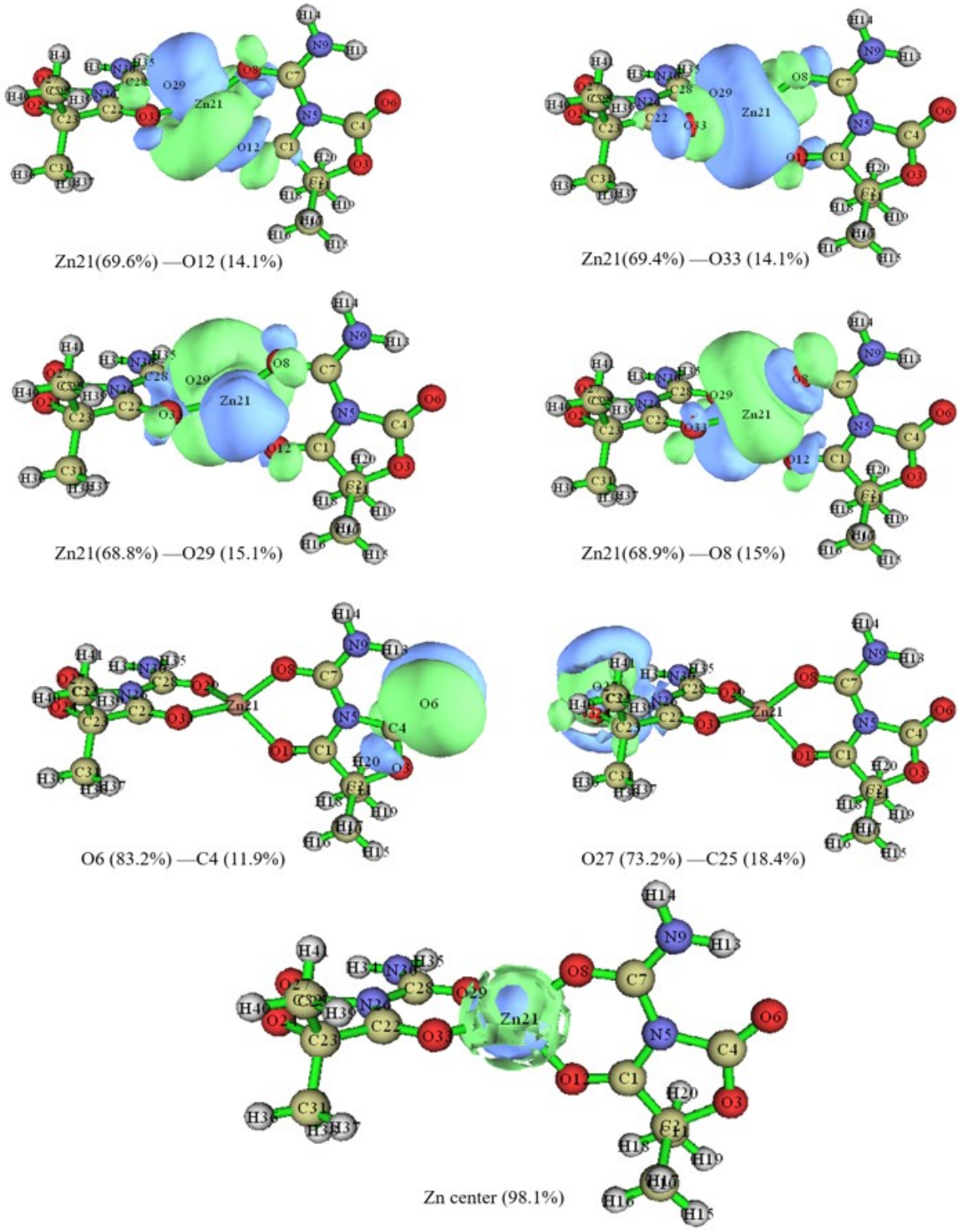

Fig. S13: Distribution of localized molecular orbitals in $Zn(Pro)_2$ system as calculated by LMO analysis.

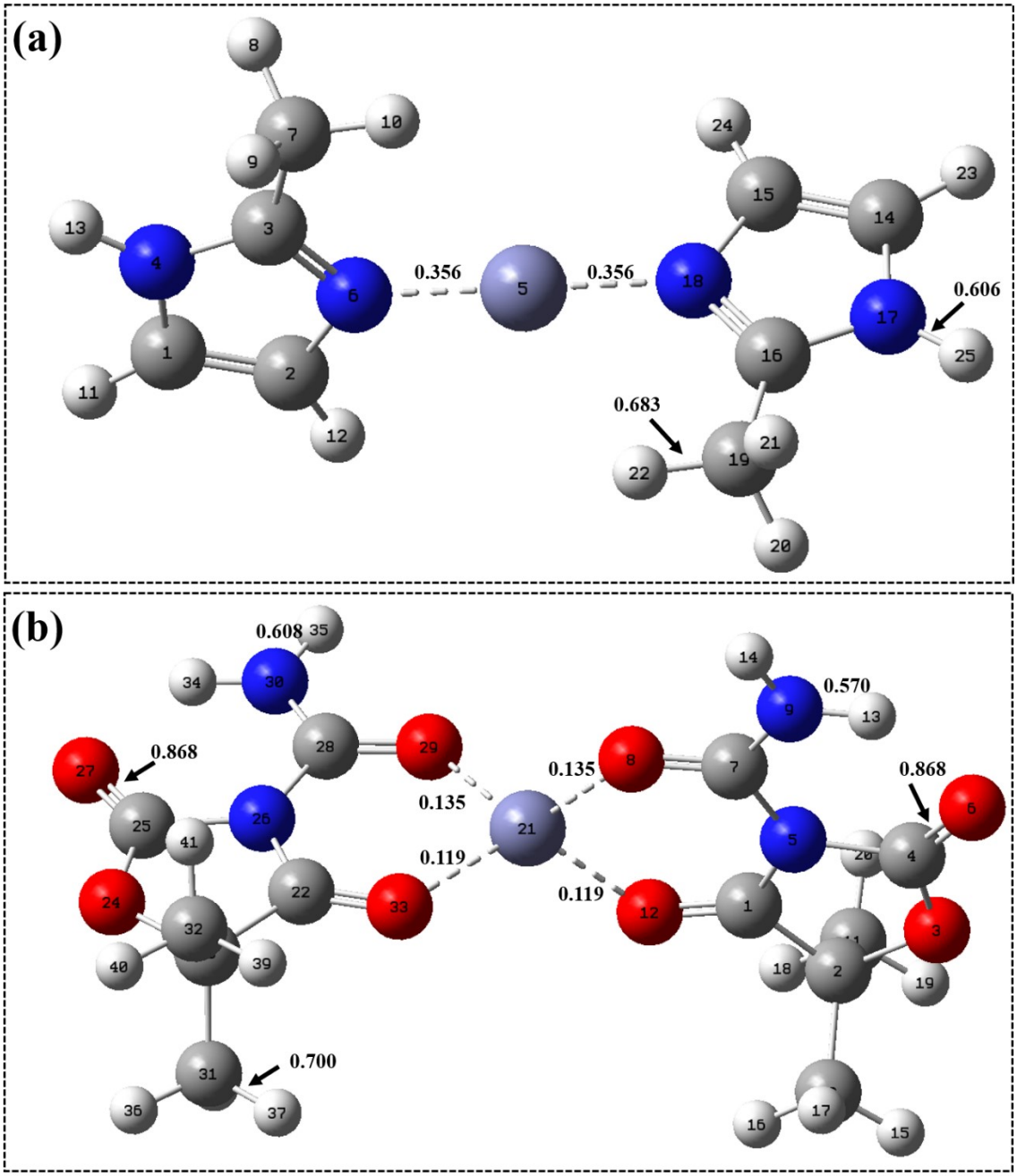

Fig. S14: Laplacian bond order (LBO) calculations for (a) $Zn(2\text{-}Mim)_2$ and (b) $Zn(Pro)_2$ systems.

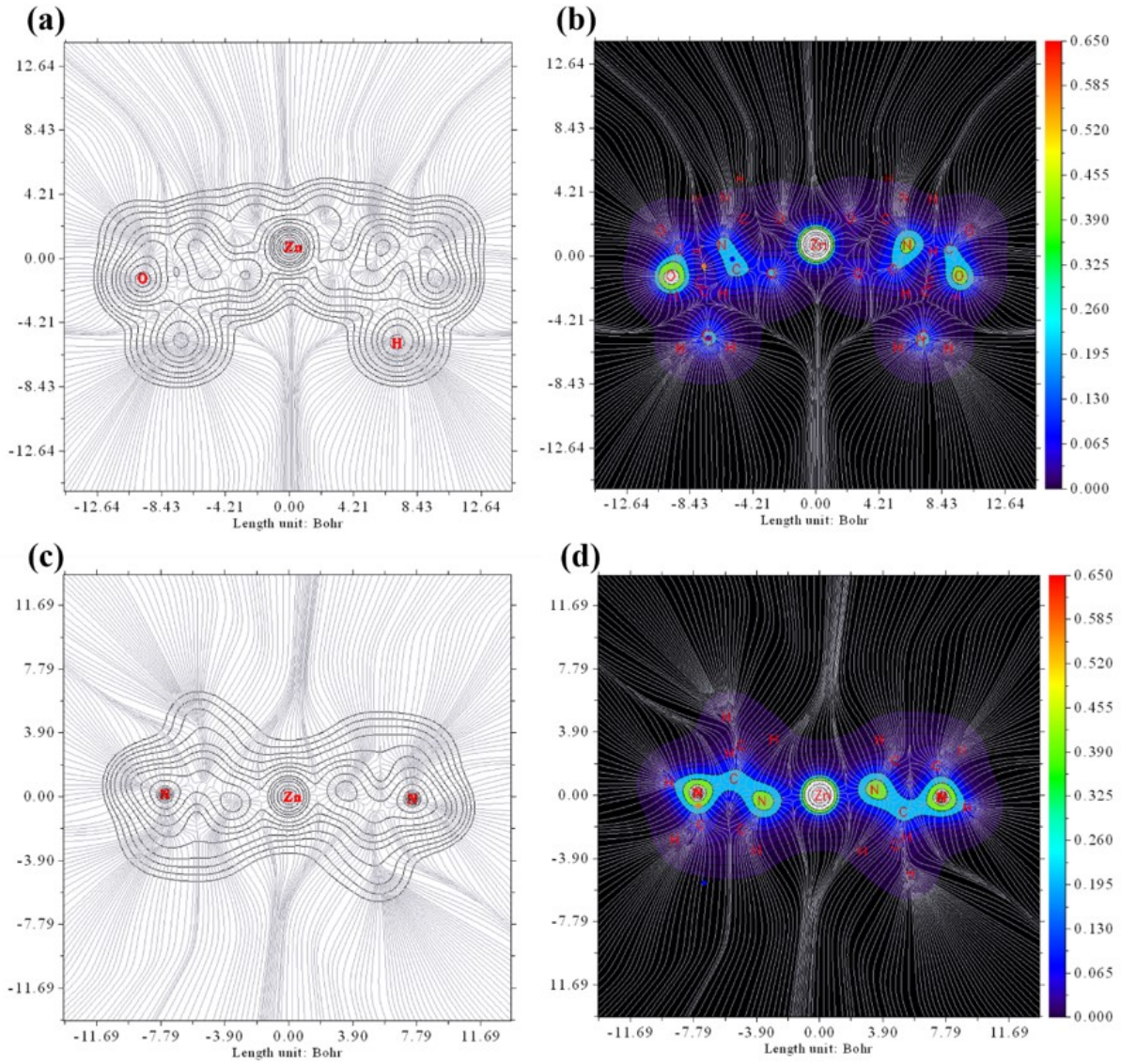

Fig. S15: (a, c) Contour line and (b, d) gradient map of Laplacian of electron density with CPs of $Zn(Pro)_2$ and $Zn(2\text{-}Mim)_2$ models on the XY plane, indicating the nature of bonding and density distribution in both systems.

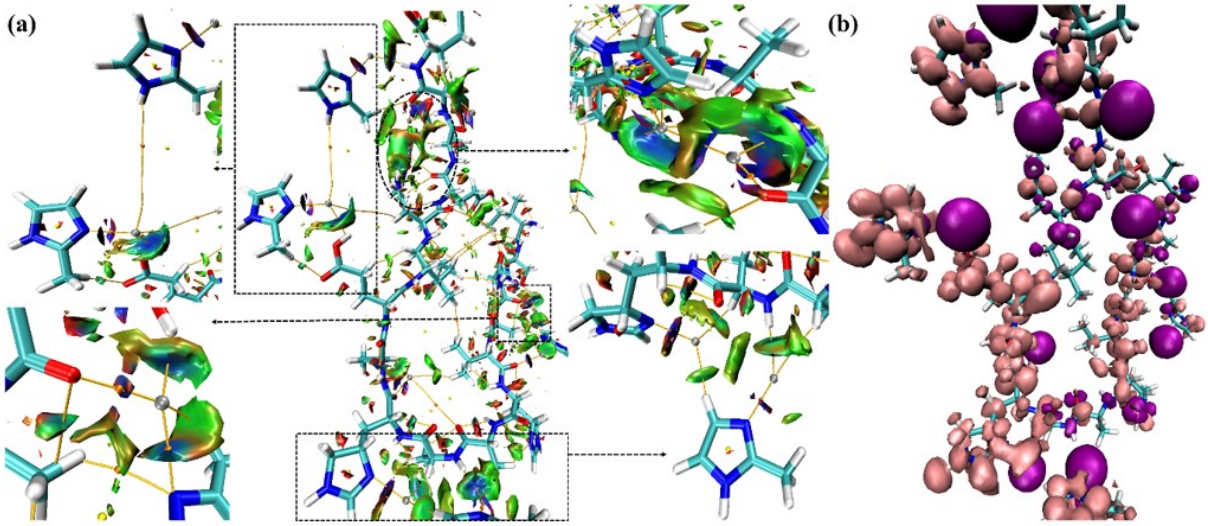

Fig. S16 : (a) Gradient isosurfaces with AIM critical points and bond paths (0.7 a.u.); specific interactions are enlarged in the insets, and (b) Orbital-weighted dual descriptor isosurface (0.001 a.u.) for large Pro-ZIF-8 system. In (a) the color scale is set to blue-green-red according to the values of sign(λ_2)ρ, ranging from −0.05 to 0.05 a.u.

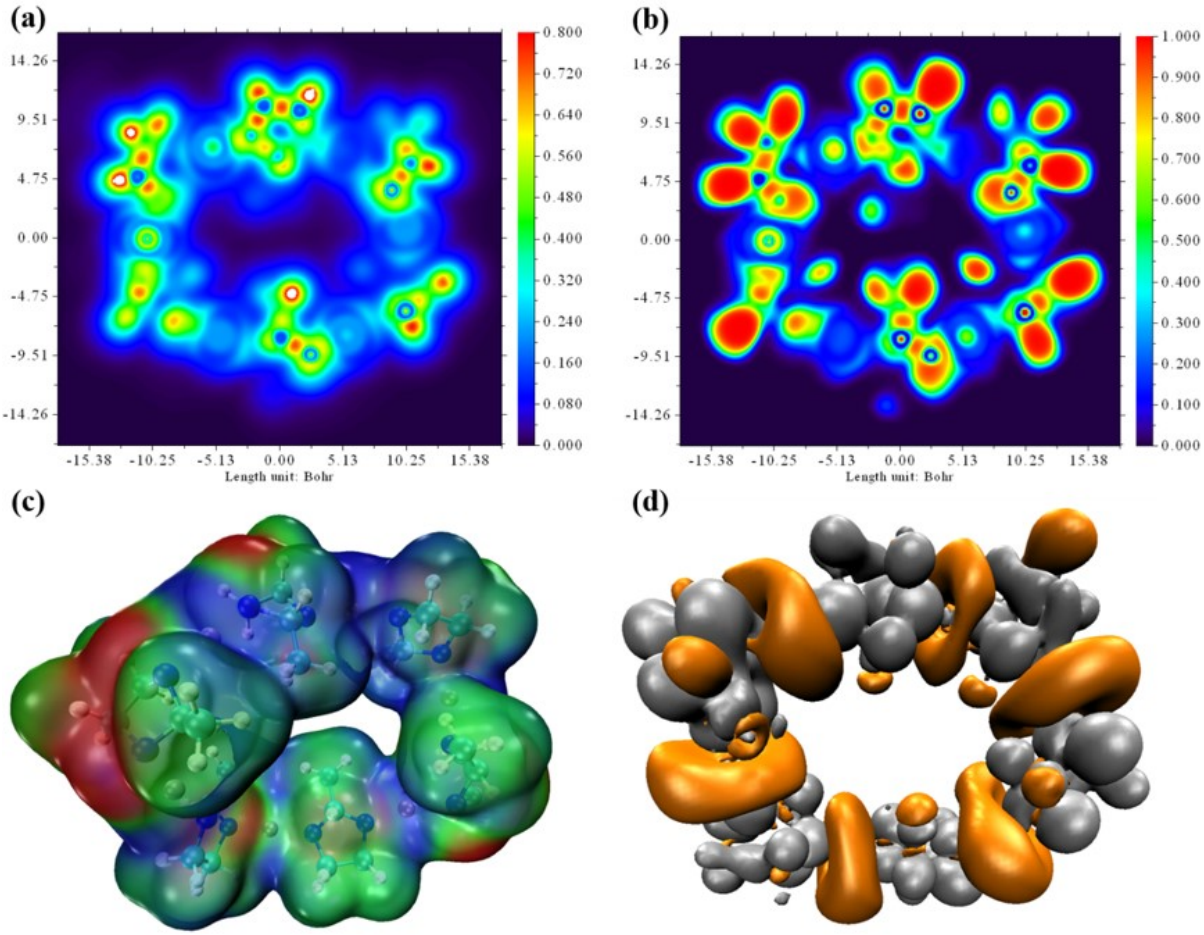

Fig. S17: Localization of electrons and the possible binding locations in the optimized ZIF-8 structure based on (a) LOL projection, (b) ELF, (c) ESP map, and (d) OWDD analyses.

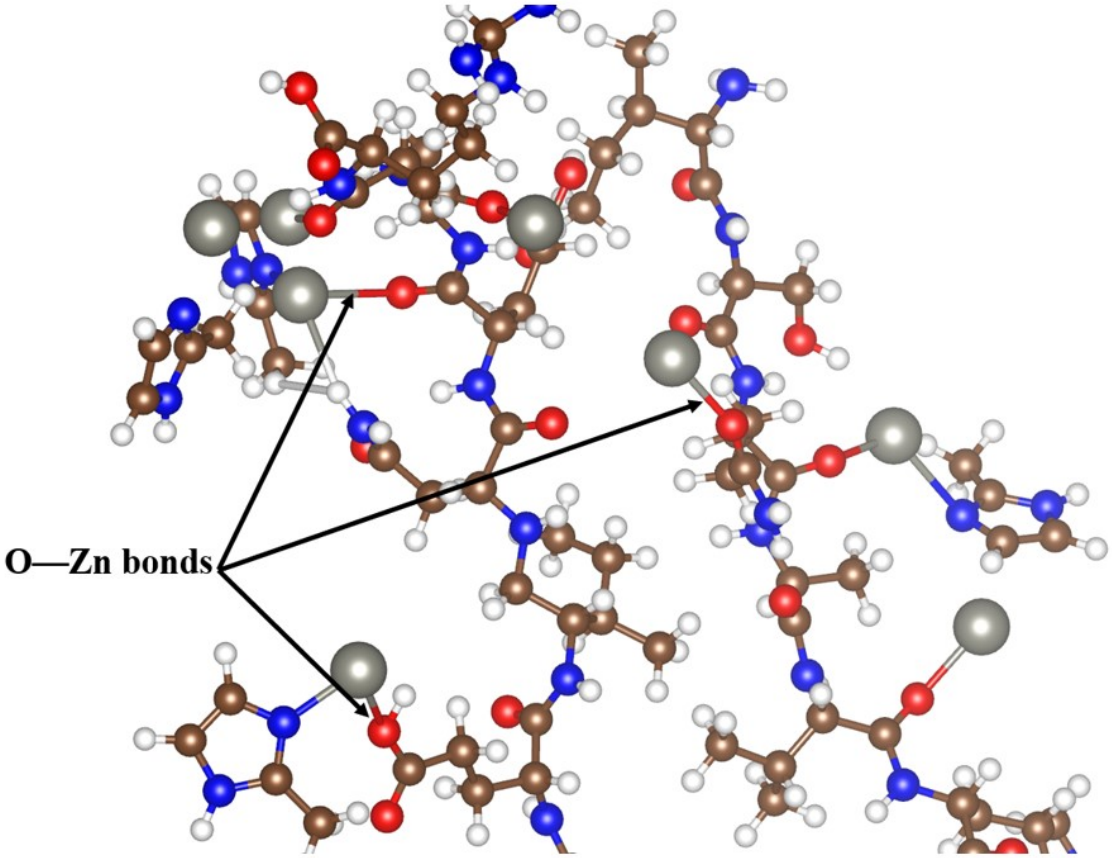

Fig. S18: Formation of strong coordination between Zn and O atoms during integration of Pro as simulated by DFT calculations.

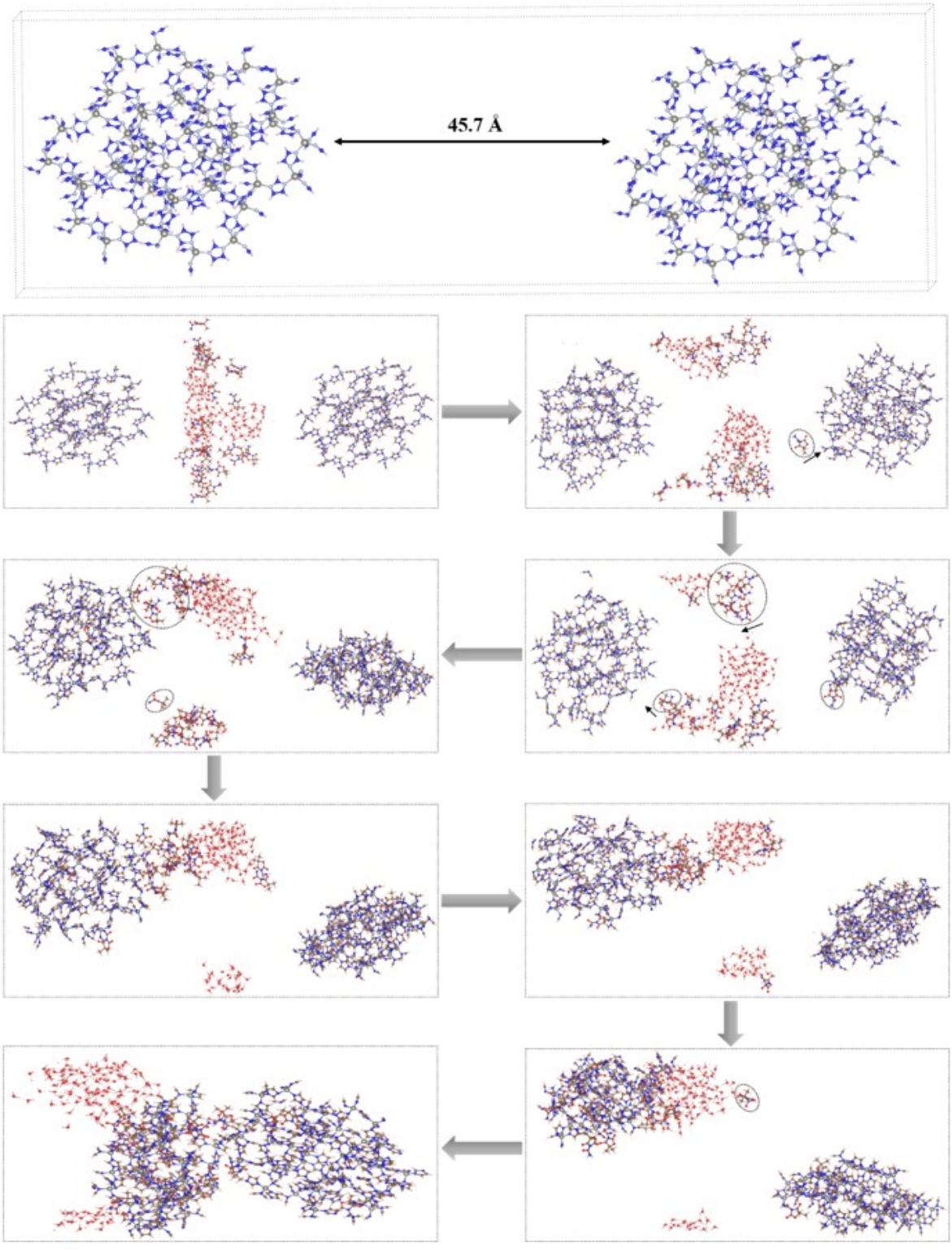

Fig. S19: Evolution of water and Pro molecules in ZIF-8 framework showing the topology and structural changes of Pro@ZIF-8 model after the encapsulation of Pro using 100000 MD steps.

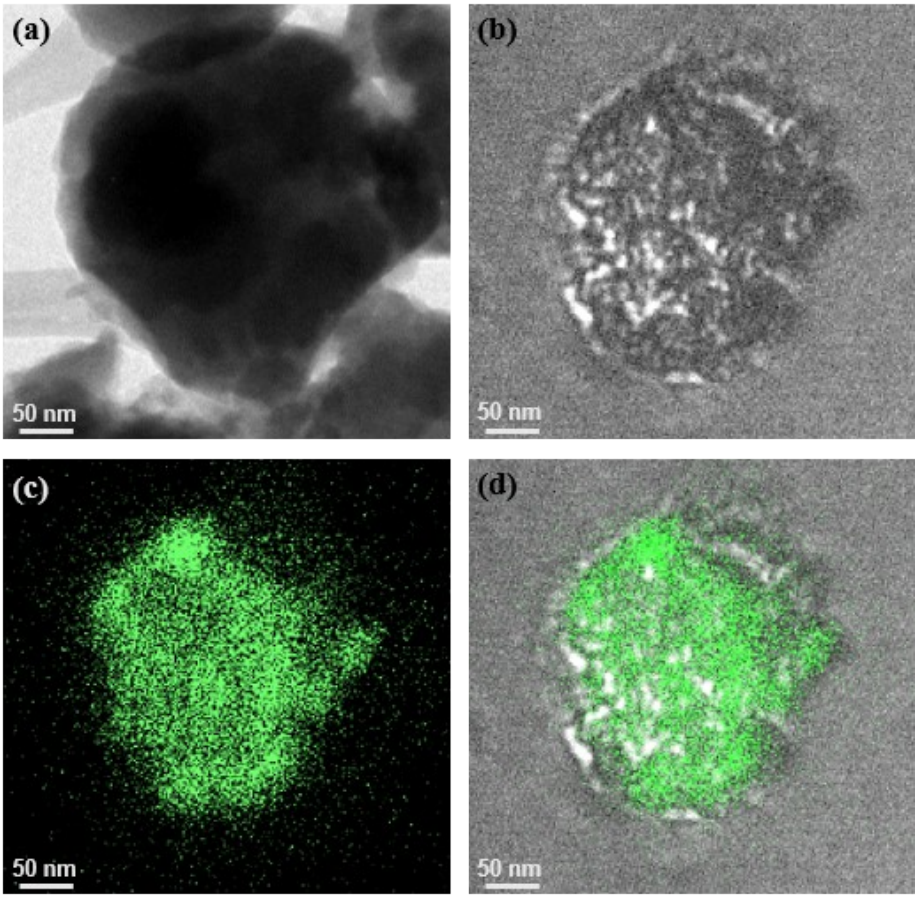

Fig. S20: (a) TEM image of encapsulated protein in ZIF-8 framework. (b) Bright-field optical image of the as-prepared nanocomposite. (c) Distribution of Pro in ZIF-8 host structure based on confocal fluorescence response. (d) Overlay result of bright-field and fluorescence images.

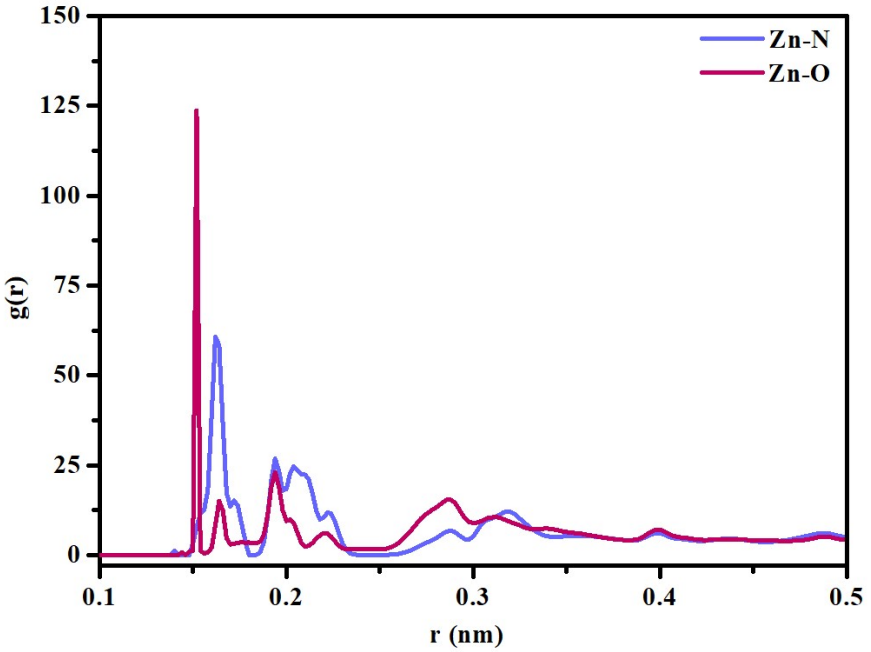

Fig. S21: Calculated radial distribution functions for O−Zn and N-Zn after 100000 MD steps.

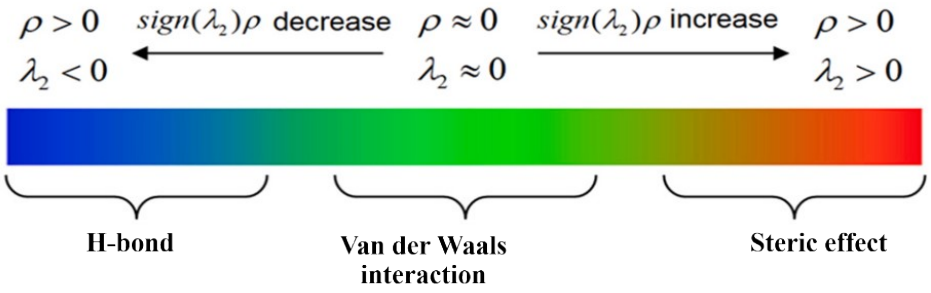

Fig. S22: Color scale bar indicating different interactions to interpret the mapped function sign(λ_2)ρ in RDG and IGM maps.

Table S1: Comparison of the catalytic activities and times of different catalysts reported using various methods in the literature.

Method	Catalyst	Reaction condition	Time (min)	Conversion (%)	Ref
Ultrasonic irradiation	Hg/Pd	$NaBH_4/H_2O$	1.5	90	[25]
Chemical co-precipitation	$Cu@Fe_2O_3@MMT$	$NaBH_4/H_2O$ /60 °C	7	96	[26]
Photochemical route	Au-Pd	$NaBH_4/H_2O$ /25 °C	40	99	[27]
Chemical reduction	Au NPs/chitosan/Fe_3O_4	$NaBH_4/H_2O$ /50 °C	2.5	81	[28]
Ligand-assisted synthesis strategy	Pd–$Fe_3O_4@SiO_2$	$NaBH_4/H_2O$ /20 °C	4	95	[29]
Hydrothermal treatment	Ag/ZnO-rGO	N_2H_4/EtOH/25 °C	120	96	[30]
Supramolecular templating method	$Ag@Me_{10}CB$	$NaBH_4/H_2O$ /25 °C	35	80	[31]
Hydrothermal treatment	Pd/Fe@γ-AlOOH-YSMs	$NaBH_4/H_2O$	3	92	[32]
Chemical treatment	Au/Au_2S–V	$NaBH_4/H_2O$	10	99	[33]
Encapsulation	Pro@ZIF-8-LDH	$NaBH_4/H_2O$	1	97	our work

Methods

Synthesis of pristine ZIF-8

In a typical fabrication procedure, ZIF-8 was synthesized as previously reported [34–36]. Briefly, 6.5 g of 2-methylimidazole (2-Mim) was dissolved in 80 mL of methanol under constant stirring, followed by the addition of 40 mL of methanol containing 3 g of $Zn(NO_3)_2 \cdot 6H_2O$ (≥98%) with vigorous stirring for a period of 24 hours. The resulting product was washed by ethanol for three times and subsequently dried at 60 °C under a vacuum for an overnight duration.

Synthesis of encapsulated Pro@ZIF-8 composite

Albumin protein (Pro) was added into 6.5 g of 2-methylimidazole under stirring at 500 rpm, followed by the addition of $Zn(NO_3)_2 \cdot 6H_2O$ aqueous solution. After stirring for 24 h, the mixture was left undisturbed for 3 h at room temperature. Finally, the prepared Pro@ZIF-8 was collected by centrifugation, washed with water and ethanol three times, and dried at 60 °C overnight.

Synthesis of 3D hollow Pro@ZIF-8-LDH material

For the synthesis of Pro@ZIF-8-LDH, two solutions are prepared. Solution A included 0.376 g of $Co(NO_3)_2 \cdot 6H_2O$ (≥98%) and 0.14 g of NH_4F, both dissolved in 50 mL of ethanol (≥99.8%) under magnetically stirring until homogeneous solution was obtained. Simultaneously, solution B was created by suspending 100 mg of Pro@ZIF-8 in 50 mL of ethanol. The two solutions are heated to 80 °C and solution A is slowly added into suspension B. The resulting mixture is refluxed at 80 °C for 1 hour and then cooled naturally. The precipitate obtained is collected, washed with ethanol and dried overnight at 60 °C to obtain Pro@ZIF-8-LDH.

Materials Characterizations

The morphologies of the synthesized materials were observed using a scanning electron microscope (SEM; Hitachi, S-4800) combined with an energy-dispersive X-ray spectrometer (EDS; Hriba EMAX) and an analytical transmission electron microscopy, equipped with an EDX spectrometer, (TEM, Philips, CM 200). Their functional groups were confirmed using Fourier transform infrared (FT-IR) spectroscopy (Perkin Elmer, Spectrum 100), and their phase composition was analyzed by Cu-Kα (0.154 nm) radiation by using a Rigaku D/MAX 2500 PC X-ray diffractometer (XRD). Confocal laser scanning microscopy (CLSM) was used to

investigate the distribution of protein structures in ZIF-8. The excitation pulses used for the analysis had a wavelength of 480 nm. The chemical components of the as-prepared materials were analyzed in detail via X-ray photoelectron spectroscopy (XPS; VG Microtech, ESCA 2000) and Raman spectroscopy (Horiba, XploRA Plus).

Theoretical calculation details

The nature of possible interactions between three target materials (Pro, ZIF-8, and LDH) based on metal-organic frameworks were investigated by conducting the density functional theory (DFT) calculations and molecular dynamic (MD) simulations. In this work, three levels of theory were used to explore the charge transfer behaviors of three distinctive materials in their frameworks, which yielded an atomic-level understanding of the interfacial mechanisms and a possible way for in-situ encapsulation of Pro to promote the ZIF-8 formation. Firstly, quantitative analyses based on electron wave functions were conducted through B3LYP hybrid functional with a 6-31G* basis set implemented in Gaussian 16 program [37]. In deep understanding about electronic structure, conjugate characteristics, covalent and noncovalent interactions as well as the donor-acceptor relationship can be visualized and quantified using the quantum theory of atoms in molecules (AIM) analysis, noncovalent interaction (NCI), reduced density gradient (RDG), average Local Ionization Energies (ALIE), independent gradient model (IGM), electron localization function (ELF), Hirshfeld surface and fingerprint plot analyses.

Secondly, MD simulations were used to understand how a protein molecule becomes embedded within the ZIF framework and help to explore the mechanism and dynamic properties of the resulting Pro@ZIF system. Briefly, in the 2 × 2 × 2 ZIF-8 cubic cell model, MD simulations in the NVT ensemble using the Nosé−Hoover thermostat with a step of 1.0 fs were run by Large-scale Atomic/Molecular Massively Parallel Simulator (LAMMPS) code. Periodic boundary conditions were applied in all three dimensions. Before MD simulations, a simulation box containing 15 proteins and 500 water molecules in the ZIF-8 cavities was relaxed to minimize the energy and to ensure that the simulation systems were sampled in an equilibrated state. After equilibration, MD simulations were run under the constant temperature (T= 300 K) and pressure (P = 0.1 MPa) and SPC/E water molecule model [38] and OPLS-AA force field [39] were adopted for the simulation system. Then, based on the equilibrium configuration of Pro@ZIF, the encapsulation of Pro and its diffusion coefficients in ZIF-8 framework at different loadings were studied.

Thirdly, and in order to further reveal the intramolecular interactions between the ZIF framework and the LDH surface for the enhanced photocatalytic activity, the first-principle DFT calculations were executed with the optimized ZIF-LDH model using the Quantum Espresso package. To describe both electronic exchange–correlation interaction and electronic wave functions, all DFT based calculations were performed using the generalized gradient approximation with Perdew-Burke-Ernzerhof exchange-correlation function (GGA-PBE) and plane wave basis set with a cut-off energy of 400 eV, respectively [40]. The hypothetical LDH model was constructed as provided in our previous work [41] and exhibits strong mutual interactions toward active organic compounds to be stable and effective for electrochemical fields. Herein, a supercell with a surface periodicity of 12 × 12 Å as a basis was used to construct the Co-LDH surface and a vacuum region of 30 Å was set in the z-direction. The Brillouin zones were sampled by employing a 2 × 2 × 1 Monkhorst-Pack k-point grid and the weak interactions were considered by Grimme-scheme empirical corrections (DFT-D). After obtaining the most stable configuration n of the ZIF-LDH system, the effect of ZIF physico-chemisorption on the LDH surface was quantitatively evaluated by calculating the adsorption energy as follows:

$$E_{ads} = E_{ZIF\ +\ LDH} - (E_{ZIF} +\ E_{LDH})$$

where $E_{ZIF+LDH}$ (eV), E_{ZIF} (eV), and E_{LDH} (eV) denote the energies of the ZIF material together with Co-LDH, ZIF framework, and Co-LDH, respectively.

Catalytic Performance

To evaluate the efficiency of as-synthesized materials for catalytic hydrogenation, 4-nitrophenol (4-NP) was used as a model nitro-compound. In the experiment, 2.5 ml of 1 mM 4-NP was mixed with 0.6 ml of freshly prepared 0.1 M $NaBH_4$. The solution's color changed from light yellow to bright yellow. Then, the mixture was transferred to a quartz cuvette and analyzed using a UV–vis spectrophotometer (Cary 5000, Agilent) at room temperature. Next, the photocatalyst was added to the solution, followed by sonication irradiation for approximately 10 seconds. The catalytic performance was monitored at predetermined time intervals by measuring the change in UV/vis absorption in the wavelength range of 240–500 nm.

References

1 Z. Chen, Y. Ha, H. Jia, X. Yan, M. Chen, M. Liu and R. Wu, *Adv. Energy Mater.*, 2019, **9**, 1803918.
2 W. Qiu, G. Li, D. Luo, Y. Zhang, Y. Zhao, G. Zhou, L. Shui, X. Wang and Z. Chen, *Adv. Sci.*, 2021, **8**, 2003400.
3 Y. Liu, Y. Wang, C. Shi, Y. Chen, D. Li, Z. He, C. Wang, L. Guo and J. Ma, *Carbon*, 2020, **165**, 129–138.
4 G. Wang, Y. Li, L. Xu, Z. Jin and Y. Wang, *Renew. Energy*, 2020, **162**, 535–549.
5 K. Wang, S. Liu, Y. Li, G. Wang, M. Yang and Z. Jin, *Appl. Surf. Sci.*, 2022, **601**, 154174.
6 Z. Li, Y. Huang, Z. Zhang, J. Wang, X. Han, G. Zhang and Y. Li, *J. Colloid Interface Sci.*, 2021, **604**, 340–349.
7 A. Chakraborty, D. A. Islam and H. Acharya, *J. Solid State Chem.*, 2019, **269**, 566–574.
8 J. Yao, R. Chen, K. Wang and H. Wang, *Microporous Mesoporous Mater.*, 2013, **165**, 200–204.
9 W. Meng, H. Wu, X. Bi, Z. Huo, J. Wu, Y. Jiao, J. Xu, M. Wang and H. Qu, *Microporous Mesoporous Mater.*, 2021, **314**, 110885.
10 Y. Luo, S. Fan, W. Yu, Z. Wu, D. A. Cullen, C. Liang, J. Shi and C. Su, *Adv. Mater.*, 2018, **30**, 1704576.
11 X. Fu, Z. Yang, T. Deng, J. Chen, Y. Wen, X. Fu, L. Zhou, Z. Zhu and C. Yu, *J. Mater. Chem. B*, 2020, **8**, 1481–1488.
12 M. Shahmirzaee, A. Hemmati-Sarapardeh, M. M. Husein, M. Schaffie and M. Ranjbar, *Microporous Mesoporous Mater.*, 2020, **307**, 110463.
13 S. Chen, X. Li, E. Dong, H. Lv, X. Yang, R. Liu and B. Liu, *J. Phys. Chem. C*, 2019, **123**, 29693–29707.
14 M. Ramezanzadeh, B. Ramezanzadeh, M. Mahdavian and G. Bahlakeh, *Carbon*, 2020, **161**, 231–251.
15 Y. Liu, Z. Li, S. Zou, C. Lu, Y. Xiao, H. Bai, X. Zhang, H. Mu, X. Zhang and J. Duan, *Int. J. Biol. Macromol.*, 2020, **155**, 103–109.
16 M. R. Ryder, B. Civalleri, T. D. Bennett, S. Henke, S. Rudić, G. Cinque, F. Fernandez-Alonso and J.-C. Tan, *Phys. Rev. Lett.*, 2014, **113**, 215502.
17 Y. Kakiuti, S. Kida and J. V. Quagliano, *Spectrochim. Acta*, 1963, **19**, 201–211.
18 M. Yang, W. Xu, Z. Chen, M. Chen, X. Zhang, H. He, Y. Wu, X. Chen, T. Zhang, M. Yan, J. Bai, C. McAlinden, K. M. Meek, J. Yu, S. Ding, R. Gao, J. Huang and X. Zhou, *Adv. Mater.*, 2022, **34**, 2109865.
19 J. Liu, J. Wang, L. Zhang, C. Fan, X. Zhou, B. Zhang, X. Cui, J. Wang, Y. Cheng and S. Sun, *J. Mater. Chem. A*, 2022, **10**, 16722–16729.
20 S. Shahrokhian, E. K. Sanati and H. Hosseini, *Nanoscale*, 2019, **11**, 12655–12671.
21 Y. Liu, X. Teng, Y. Mi and Z. Chen, *J. Mater. Chem. A*, 2017, **5**, 24407–24415.
22 Y.-T. Liu, X. Chen, J. Yu and B. Ding, *Angew. Chem. Int. Ed.*, 2019, **58**, 18903–18907.
23 S. Wang, H. Yao, S. Sato and K. Kimura, *J. Am. Chem. Soc.*, 2004, **126**, 7438–7439.
24 J. Liu, H. Bai, Y. Wang, Z. Liu, X. Zhang and D. D. Sun, *Adv. Funct. Mater.*, 2010, **20**, 4175–4181.
25 V. K. Harika, H. K. Sadhanala, I. Perelshtein and A. Gedanken, *Ultrason. Sonochem.*, 2020, **60**, 104804.
26 B. Zeynizadeh, S. Rahmani and H. Tizhoush, *Polyhedron*, 2020, **175**, 114201.
27 P. Fageria, S. Uppala, R. Nazir, S. Gangopadhyay, C.-H. Chang, M. Basu and S. Pande,

Langmuir, 2016, **32**, 10054–10064.
28 Y. Qiu, Z. Ma and P. Hu, *J. Mater. Chem. A*, 2014, **2**, 13471–13478.
29 M. An, J. Cui and L. Wang, *J. Phys. Chem. C*, 2014, **118**, 3062–3068.
30 B. Paul, S. Vadivel, N. Yadav and S. S. Dhar, *Catal. Commun.*, 2019, **124**, 71–75.
31 H.-F. Li, J. Lü, J.-X. Lin and R. Cao, *Inorg. Chem.*, 2014, **53**, 5692–5697.
32 X. Cui, Y. Zheng, M. Tian and Z. Dong, *Appl. Surf. Sci.*, 2017, **416**, 103–111.
33 B. Gadgil, P. Damlin, A. Viinikanoja, M. Heinonen and C. Kvarnström, *J. Mater. Chem. A*, 2015, **3**, 9731–9737.
34 X. Zhang, C. Xu, S. Li, X. Liu and Y. Liu, *Appl. Mater. Today*, 2021, **25**, 101228.
35 Y. Tang, H. Li, R. Zhang, W. Guo and M. Yu, *ACS Omega*, 2021, **6**, 28528–28537.
36 S. Z. N. Ahmad, W. N. W. Salleh, N. Yusof, M. Z. M. Yusop, R. Hamdan and A. F. Ismail, *Appl. Nanosci.*, 2022, 1–15.
37 M. Frisch, G. Trucks, H. Schlegel, G. Scuseria, M. Robb, J. Cheeseman, G. Scalmani, V. Barone, G. Petersson and H. Nakatsuji, *Wallingford CT*.
38 H. J. C. Berendsen, J. R. Grigera and T. P. Straatsma, *J. Phys. Chem.*, 1987, **91**, 6269–6271.
39 W. L. Jorgensen, J. Chandrasekhar, J. D. Madura, R. W. Impey and M. L. Klein, *J. Chem. Phys.*, 1983, **79**, 926–935.
40 J. Perdew, K. Burke and M. Ernzerhof, *Phys. Rev. Lett.*, 1998, **80**, 891.
41 M. Chafiq, A. Chaouiki, T. Suhartono, F. Hazmatulhaq and Y. Gun Ko, *Chem. Eng. J.*, 2023, 142239.